PHYSICAL REVIEW C **66**, 014608 (2002)

Near-scission emission of intermediate mass fragments in $^{12}\mathrm{C}+{}^{232}\mathrm{Th}$ at $E/A=16$ and 22 MeV

T. A. Bredeweg, R. Yanez,* B. P. Davin, K. Kwiatkowski,† and R. T. de Souza
Department of Chemistry and Indiana University Cyclotron Facility, Indiana University, Bloomington, Indiana 47405

R. Lemmon‡ and R. Popescu§
National Superconducting Cyclotron Laboratory and Department of Physics and Astronomy, Michigan State University, East Lansing, Michigan 48824

R. J. Charity and L. G. Sobotka
Department of Chemistry, Washington University, St. Louis, Missouri 63130

D. Hofman‖
Physics Division, Argonne National Laboratory, Argonne, Illinois 60439

N. Carjan
Centre d'Etudes Nucléaires de Bordeaux-Gradignan, BP 120, F-33175 Gradignan Cedex, France

(Received 25 July 2001; published 17 July 2002)

Intermediate mass fragments (IMFS) (IMF: $3\leq Z_{\mathrm{IMF}}\leq 20$) observed in coincidence with two correlated fission fragments following incomplete fusion in $^{12}\mathrm{C}+{}^{232}\mathrm{Th}$ at $E/A=16$ and 22 MeV are investigated. IMFs emitted prior to significant deformation of the fissioning system, as well as IMFs emitted near scission, are distinguished based upon their characteristic kinetic energy and angular distributions. The yield distributions of IMFs emitted near scission in these $^{12}\mathrm{C}$ induced reactions are compared with near-scission IMF yields in spontaneous and low-energy ternary fission. Comparisons are made to both experimental fusion-evaporation data and theoretical predictions of a statistical model. The excitation energy dependence of relative IMF yields for both isotropic and near-scission emission is also presented. Our results for near-scission emission suggest that the production of IMFs near scission is inconsistent with a statistical emission mechanism in which emission barriers follow a standard Z dependence. Dynamical model calculations are used to investigate the role of dissipation, angular momentum, N/Z, and kinetic energy on the fragment formation near scission.

DOI: 10.1103/PhysRevC.66.014608 PACS number(s): 25.70.Jj, 25.85.Ge, 47.20.Dr

I. INTRODUCTION

Nuclear fission is a fascinating process as it involves the shape instability of a small, strongly interacting system of a few hundred constituents [1,2]. This splitting of the nuclear droplet, which involves the collective rearrangement of the constituent nucleons, can be described as a surface instability [3]. The details of how such shape instabilities proceed for small, strongly interacting systems, particularly at finite temperature, remains an open question. Since the instability is a surface instability, the general phenomenological approach has been to describe the fission process in terms of an evolution of the shape of the liquid drop. As the instability is governed by the interplay between the Coulomb and surface energies, a leptodermous liquid-drop-type model captures the relevant physics. It is well established that as the nucleus deforms from a mononucleus to a dinuclear system, nuclear dissipation couples the shape degrees of freedom to the intrinsic excitation of the system. The nature of this dissipation, both its magnitude and its tensorial properties, is a subject of widespread interest. One suggested probe to study nuclear dissipation is ternary fission, in which the nuclear system splits into three fragments [4]. As the yield for ternary fission is small compared to binary fission, a model which describes not just the average behavior but the fluctuations within the system is required. The present experimental data hopefully provide the stimulus for the development of such a theoretical model, as well as the appropriate comparison for the predictions of such a model.

In nuclear fission, a few probes of dissipation exist: the total kinetic energy of the fission fragments, the prescission neutron multiplicity, the multiplicity of giant dipole resonance (GDR) γ rays, and near-scission charged particle emission. The systematics of the total kinetic energies of the fission fragments has received considerable attention over the past few decades [5,6] and is relatively well understood phenomenologically. The use of the prescission neutron multiplicity as a "neutron clock" to investigate the descent of the system from saddle to scission has also received considerable attention [7]. However, the problem of distinguishing between neutrons emitted prior to the system attaining its saddle configuration and neutrons emitted as the system evolves between saddle and scission configurations limits the applicability of this approach. GDR γ rays have also re-

---

*Present address: Universidad de Chile, Santiago, Chile.

†Present address: Los Alamos National Lab., Los Alamos, NM.

‡Present address: CCLRC Daresbury Laboratory, Warrington, WA4 4AD UK.

§Present address: Brookhaven National Laboratory, Upton, NY.

‖Present address: University of Illinois at Chicago, Chicago, IL.

ceived considerable attention as a probe of the nuclear viscosity [8,9]. As with prescission neutrons however, present ambiguities as to the yield of γ rays emitted presaddle vs postsaddle limit the usefulness of this probe of fission dynamics. In contrast, near-scission charged particle emission (ternary fission), for hot systems, has received relatively little attention as a probe of fission dynamics and thus presents an unique opportunity.

In this work we present the results of two ^{12}C induced reactions on ^{232}Th targets at $E/A=16$ and 22 MeV. In Sec. II we describe the experimental setup and the detector calibrations. The main experimental results of this work are presented in Sec. III. In Sec. IV we describe our calculations with the Los Alamos macroscopic dynamical model for large amplitude collective motions to investigate the influence of angular momentum, N/Z, and kinetic stretching on ternary fission. Section V presents an attempt to describe our results in terms of statistical emission theory. The conclusions of our present work are summarized in Sec VI. Details of the kinematic reconstruction program and the efficiency calculations are found in Appendixes A and B, respectively. All data shown unless explicitly stated otherwise are corrected by both the kinematic reconstruction and geometric efficiency procedures.

II. EXPERIMENTAL SETUP

Two independent experiments were performed, one at Michigan State University (MSU) and the other at Argonne National Laboratory (ANL), in which a ^{12}C beam accelerated to energies of $E/A=22$ MeV ($E_{\rm lab}=264$ MeV) and $E/A=16$ MeV ($E_{\rm lab}=193$ MeV) by the K1200 cyclotron and the Atlas linac, respectively, bombarded a self-supporting 700 μg/cm^2 ^{232}Th target. The average intensity of the beam was $\sim 1-4\times 10^{10}$ particles per sec. Both experiments utilized an almost identical physical setup which is schematically illustrated in Fig. 1. Differences in detector placement, mandated by the slightly different kinematics, are summarized in Table I and Table II. Target shadowing was minimized by rotating the target foil ~45° with respect to the beam axis.

Fission fragments were detected by pairs of hybrid large area parallel plate avalanche counter/multiwire proportional counters (PPACs), one on either side of the beam axis, as shown in Fig. 1. One pair of PPACs was centered at beam height [the (y,z) plane] while one or two additional pairs were rotated out of the (y,z) plane by an angle $\varphi=\pm 27.5°$ directly above or below the center PPACs. Situated at a distance of 30 cm from the target, each PPAC, with an active area of 8 cm×14 cm, provided an angular coverage of $\sim 32°$ in $\theta_{\rm lab}$. The x and y position sensitivity was provided by two parallel wire planes with the wires oriented in mutually orthogonal directions. The anode provided a timing signal with a rise time of 4–5 ns for fission fragments. This fast signal in conjunction with the accelerator radio frequency allowed measurement of the fission-fragment velocities. The position of an ionizing particle in the PPAC in both the x and y directions was determined by the standard delay line technique [10–12]. The PPACs were operated at a gas pressure of ~4 Torr of isobutane and an applied voltage of ~550 V. Previous tests indicated that these conditions result in almost unit efficiency for detecting fragments with $Z\geqslant 8$ [13]. The described experimental setup provided measurement of the fission-fragment folding angle in the range $128°\leqslant\theta_{\rm AB}\leqslant 178°$ for the MSU experiment and $128°\leqslant\theta_{\rm AB}\leqslant 180°$ in the ANL experiment.

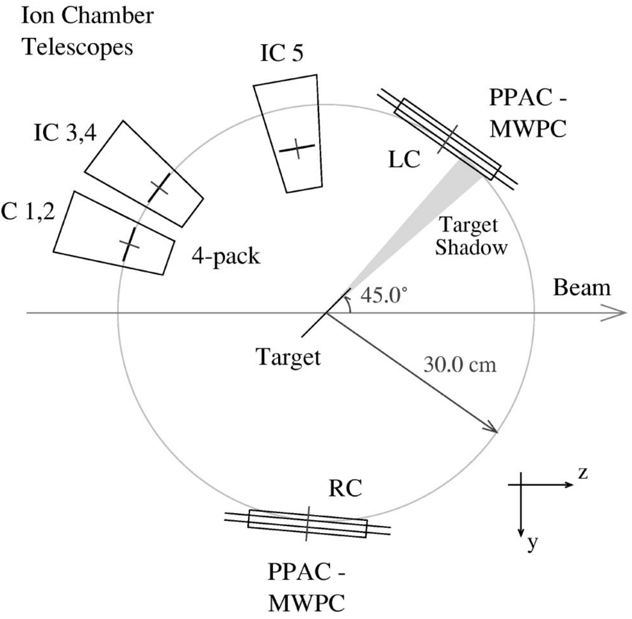

FIG. 1. Experimental setup used to investigate the reactions ^{12}C+^{232}Th at $E/A=16$ and 22 MeV.

The position resolution achieved with the PPACs is shown in Fig. 2. In Fig. 2(a), single wire resolution in the x direction is evident. As this wire plane is in the multiwire portion of the counter, collection of electrons on the x wires themselves results in the excellent resolution. Position resolution in the y direction is somewhat worse as can be seen in Fig. 2(b), as it relies on an induced rather than a direct signal. The resolution (~0.5°) evident in Fig. 2 is sufficient for measuring the fission-fragment angular correlations as postscission neutron emission alters these correlations by ~2° on average. Position signals from the PPAC detectors were calibrated by using a ^{252}Cf fission source, a set of precisely machined masks, and an optical transit. The calibration procedure provided unambiguous position assignment of

TABLE I. Angular positions of the parallel plate avalanche counter (PPAC) during the two experiments.

	$E/A=22$ MeV		$E/A=16$ MeV	
PPAC	ϑ	φ	ϑ	φ
Left-Center	+51.3°	0.0°	+55.0°	0.0°
Right-Center	−95.2°	0.0°	−95.0°	0.0°
Left-Up	+51.3°	+27.5°	+55.0°	+27.5°
Right-Down	−95.2°	−27.5°	−95.0°	−27.5°
Left-Down	+51.3°	−27.5°	n/a	n/a
Right-Up	−95.2°	+27.5°	n/a	n/a

TABLE II. Angular positions of the ion chamber telescopes during the two experiments.

Telescope number	$E/A=22$ MeV ϑ	$E/A=22$ MeV φ	$E/A=16$ MeV ϑ	$E/A=16$ MeV φ
1	+167.6°	+8.8°	+160.8°	−8.8°
2	+167.6°	−8.8°	+160.8°	+8.8°
3	+149.9°	−8.8°	+143.2°	+8.8°
4	+149.9°	+8.8°	+143.2°	−8.8°
5	+100.6°	0.0°	+100.0°	0.0°

the wires in each PPAC. The position signals for two coincident particles allowed selection of correlated fission fragments on the basis of coplanarity. The anode signal of the PPAC was also used to provide a measure of the pulse height. Based upon their significantly larger pulse height, fission fragments were cleanly distinguished from α particles in the off-line analysis.

Charged particles emitted in the reactions were detected with low-threshold ionization chamber/Si(IP)/CsI(Tl) telescopes [14,15]. The angular location of the center of each telescope in both experiments is listed in Table II. The ionization chambers were operated at a pressure of ~18 Torr of CF_4, providing a ΔE measurement with a low detection threshold (~0.8 MeV/nucleon). The Si(IP) detector present in each telescope was 300 μm thick, sufficient to stop all charged particles with $Z\geqslant 3$ emitted in these reactions, providing an E_{resid} measurement. The Si(IP) consisted of a quadrant design (2.5 cm×2.5 cm/quadrant), thus providing an angular quantization of ~5° for detection of intermediate mass fragments (IMFs) and light charged particles (LCPs). Each quadrant of the Si(IP) detector was backed by a CsI(Tl)/PD detector, which was used to veto energetic charged particles that "punched through" the Si(IP) detector.

Energy calibration of the ion chamber (IC) telescopes was performed using a ^{228}Th α source at the target position. The linearity of the Si(IP) detectors, together with the associated electronics, was checked over the full dynamic range of the analog-to-digital converters by injecting a series of precisely controlled charge pulses at the input of each charge sensitive preamplifier. The α-source calibration together with the electronic pulser provided an absolute energy calibration. All dead layers, including the measured dead layer on the front face of the Si(IP) detector, were accounted for in the off-line analysis with an energy loss program [16,17]. The atomic number, Z, of particles traversing the IC telescopes was determined by utilizing the ΔE-E technique [18].

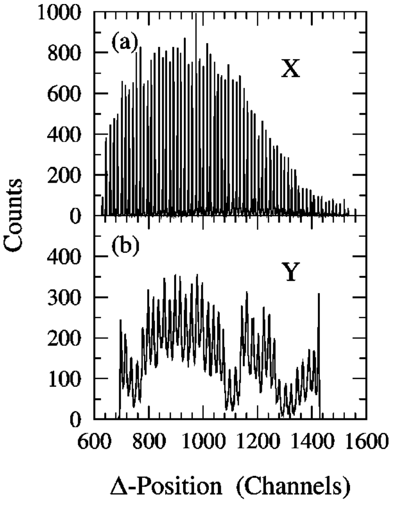

FIG. 2. Position resolution in the x and y directions for the PPAC-MWPC.

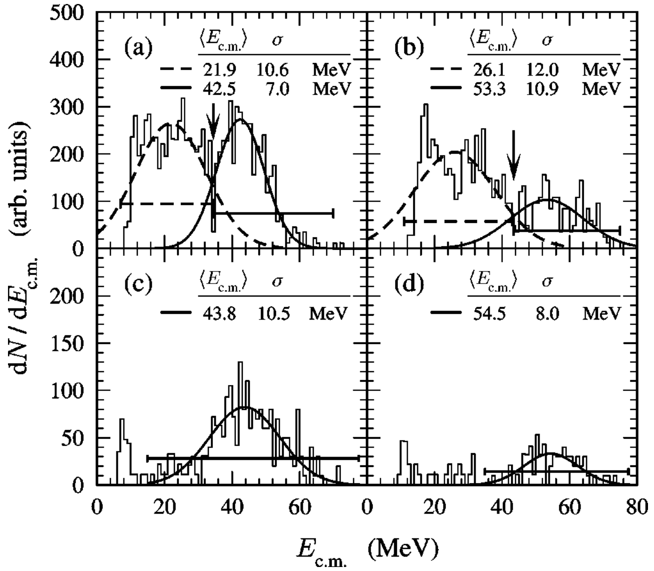

FIG. 3. Kinetic energy distributions of Be [(a) and (c)] and C [(b) and (d)] fragments observed in ternary fission events. The data in (a) and (b) are measured ~90° from the scission axis while the data in (c) and (d) are measured ~50° from the scission axis. Horizontal bars denote the fit regions used.

Both binary (two coincident PPACs) and ternary events (two coincident PPACs and an IC telescope) were recorded for off-line analysis. Binary events were downscaled by a factor between 10 and 20 to reduce the dead time of the data acquisition system.

III. EXPERIMENTAL RESULTS

The center-of-mass kinetic energy distributions for fragments detected in coincidence with two correlated fission fragments in the reaction ^{12}C+^{232}Th at $E/A=22$ MeV are displayed in Fig. 3. Figures 3(a) and 3(b) depict the energy spectra for beryllium and carbon fragments, respectively, as measured ~90° with respect to the scission axis (IC 1–IC 4 in Fig. 1). Both distributions are bimodal, in agreement with earlier investigations of ternary fission [19,20]. The energy spectra for beryllium and carbon fragments, as measured ~50° with respect to the scission axis, are shown in Figs. 3(c) and 3(d) (IC 5 in Fig. 1). Unlike the ~90° spectra, these distributions are single peaked. Gaussian fits to the high-energy component in Figs. 3(c) and 3(d) yielded mean center-of-mass energies, $\langle E_{\mathrm{c.m.}}\rangle$, of 43.8 MeV for beryllium and 54.5 MeV for carbon. These values of the $\langle E_{\mathrm{c.m.}}\rangle$ are close to the values obtained for the high-energy component at angles orthogonal to the scission axis [Figs. 3(a) and 3(b)].

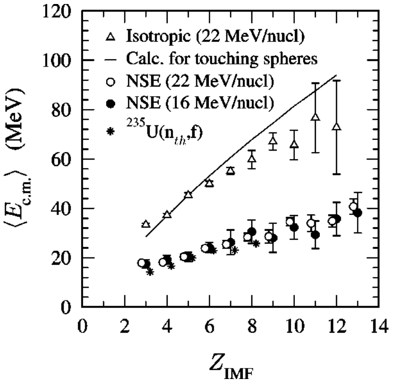

FIG. 4. Dependence of the average center-of-mass kinetic energy on the atomic number of the ternary particle, Z_{IMF}. Data for $^{235}\mathrm{U}(n_{th},f)$ are taken from Ref. [29].

In this latter case, fits to the high-energy components yielded values of 42.5 MeV for beryllium and 53.3 MeV for carbon, respectively. In addition, the overall yield of the high-energy component, after accounting for the difference in detector solid angle, is comparable between the two angular regions. These results are therefore indicative of an emission mechanism which is isotropic or close to it. A reasonable and consistent scenario is that the high-energy component is associated with prescission emission from a system which has not proceeded, as of the emission time, far along its ultimate fission trajectory.

The low-energy component, in contrast, corresponds to emission near the moment of scission from the region between the two nascent fission fragments—the neck. Near cancellation of Coulomb forces parallel to the scission axis results in the ternary particle being propelled essentially perpendicular to the scission axis giving near-scission emission (NSE) its characteristic energy-angle relationship [21].

To distinguish between isotropic and near-scission emission in ternary fission events, we have applied simple one-dimensional cuts to the kinetic energy distributions, as shown by the arrows in Fig. 3. We have assessed the "contamination" between the low-energy near-scission emission and the high-energy isotropic emission due to this simple selection by utilizing more restrictive energy selection criteria. These more restrictive criteria do not alter our conclusions. Due to the limited statistics, most of the analysis was performed with the less restrictive energy cuts denoted by the arrows in Fig. 3.

The dependence of the average kinetic energy on the Z_{IMF} of the emitted ternary fragment is depicted in Fig. 4. Both the isotropic and near-scission components exhibit a roughly linear dependence of the average energy on Z_{IMF}. The solid line indicates the Coulomb barrier for a touching-spheres scenario given by

$$E_c = \frac{1.44 Z_{\mathrm{IMF}}(Z_{\mathrm{source}} - Z_{\mathrm{IMF}})}{1.4[A_{\mathrm{IMF}}^{1/3} + (A_{\mathrm{source}} - A_{\mathrm{IMF}})^{1/3}] + 2}\,\mathrm{MeV}, \qquad (1)$$

where Z_{source} and A_{source} have been assumed to be 90 and 232, respectively, to roughly account for incomplete fusion and prescission emission of neutrons. The kinetic energies for isotropically emitted fragments are roughly consistent with this simple formula, indicating that these fragments are emitted while the excited composite system is still relatively compact and spherical, consistent with a statistical emission scenario. The enhanced bend over (relative to the calculation) of $\langle E_{\mathrm{c.m.}} \rangle$ for large values of Z_{IMF} may be due to the effects of shape polarization [22] or shape fluctuations [23]. In contrast to statistical emission from a spherical source, fragments emitted near scission have significantly lower average kinetic energies consistent with emission from a distended source on a time scale commensurate to the fission process. As evident in Fig. 4, the magnitude of $\langle E_{\mathrm{c.m.}} \rangle$ for near scission emission at 22 MeV, 16 MeV, and even thermal neutron induced fission of ^{235}U is essentially the same. This result may indicate that the average kinetic energy of the fragments emitted near scission depend weakly, if at all, on the excitation of the system. This behavior should be compared with the average kinetic energies of evaporated particles which depend on the temperature of the emitting system. Unfortunately the quality of the experimental data does not allow us to make a detailed comparison. The constancy of the $\langle E_{\mathrm{c.m.}} \rangle$ for the NSE component for different incident energies and projectiles may also arise from the fact that although the *initial* excitation energy in the three cases is quite different, the excitation energy at the time of near-scission emission is comparable.

TABLE III. Average azimuthal correlation angles, corrected for finite detector resolution, for binary and ternary fission in the two reactions along with their associated second moments.

Incident energy	$\langle \phi_{\mathrm{AB}} \rangle_{\mathrm{binary}}$	$\langle \phi_{\mathrm{AB}} \rangle_{\mathrm{ternary}}$
$E/A = 22$ MeV	180.1° ($\mu_2 = 16.0°$)	180.3° ($\mu_2 = 17.9°$)
$E/A = 16$ MeV	180.6° ($\mu_2 = 14.0°$)	181.0° ($\mu_2 = 15.2°$)

In order to fully understand the characteristics of ternary fission, it is important to compare the angular correlations between fission fragments with the case of binary fission. The coplanarity angle, ϕ_{AB}, defined as the difference between the azimuthal coordinates of the two coincident fission fragments, i.e., $\phi_{\mathrm{AB}} = |\phi_{\mathrm{A}} - \phi_{\mathrm{B}}|$, provides useful information regarding the conservation of linear momentum between the two fission fragments in the transverse direction. Conservation of linear momentum between the two fission fragments requires that the angle ϕ_{AB} equal 180°. Table III lists the mean values of ϕ_{AB} and second moments σ^2, obtained by fitting a Gaussian to each of the distributions shown in Fig. 5. The mean value in all four cases is effectively equal to 180°, indicating conservation of transverse momentum. The width of the coplanarity angular distribution reflects both momentum transfer perpendicular to the beam axis in the incomplete fusion reaction and postscission neutron or charged particle evaporation. Both the binary distributions and the ternary distributions (with $Z_{\mathrm{IMF}} \geqslant 3$) shown in Figs. 5(a) and 5(b), respectively, have comparable means and widths. In the current work, the azimuthal correlation was primarily used to verify the correlation of two fission frag-

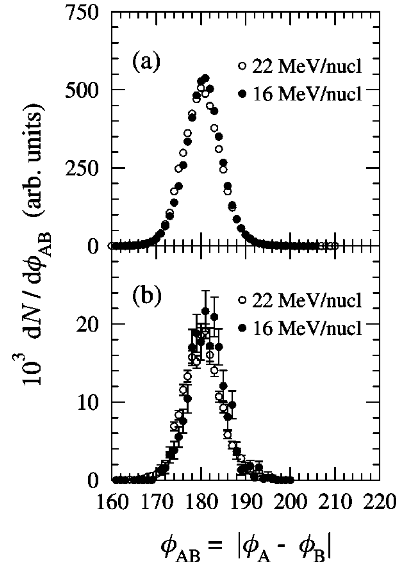

FIG. 5. Distribution of the coplanarity angle ϕ_{AB} for binary (a) and ternary (b) events. In the ternary case, $Z \geqslant 3$ for the ternary particle.

ments. As described in Appendix B, it was also used to estimate the impact of postscission neutron emission on the measured folding angle.

The linear momentum transferred to the composite system from the incident projectile can be determined by examining the fission-fragment folding angle $\theta_{AB} = \theta_A + \theta_B$ between two correlated fission fragments [24]. At low incident energies, complete fusion is the dominant interaction mechanism and a central collision between projectile and target nuclei transfers all of the momentum of the incident projectile to the composite nucleus. On the other hand, a more peripheral interaction will result in the transfer of considerably less linear momentum. The larger the transferred momentum, the higher the velocity of the fissioning system. Since the two fission fragments are emitted back to back in their center-of-mass frame when fission occurs, the higher the velocity of the fissioning system the smaller the folding angle of the two fission fragments in the laboratory frame. The measured fission-fragment folding angle distributions for both binary and ternary fission are presented in Fig. 6.

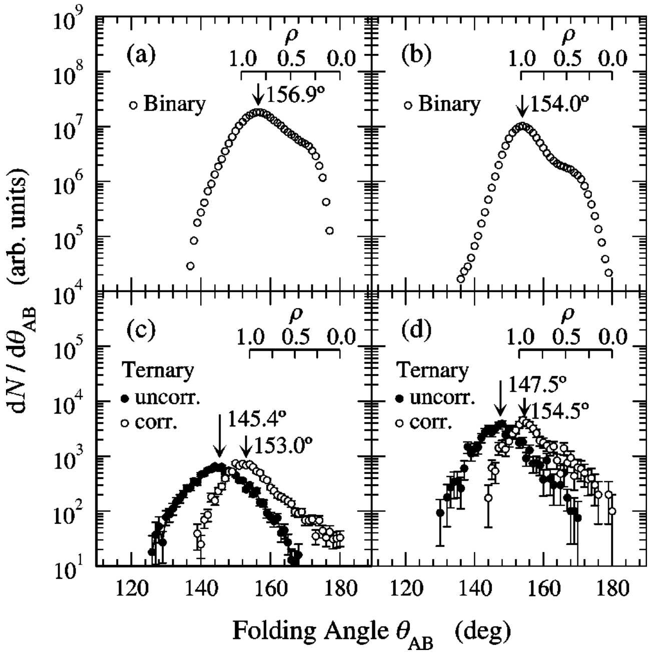

FIG. 6. Folding angle distribution θ_{AB} for coincident fission fragments at $E/A = 22$ MeV [(a) and (c)] and 16 MeV [(b) and (d)] in binary and ternary fission. For ternary fission, solid symbols represent the measured folding angles and open symbols indicate the folding angle following recoil correction. A fractional linear momentum transfer scale, $\rho = p_{\parallel}/p_{\mathrm{beam}}$, is included in each panel.

Displayed in Figs. 6(a) and 6(b) are the binary folding angle distributions for both incident energies. These distributions exhibit a dominant peak which can be approximated with a Gaussian with a most probable value of 156.9° for the 22 MeV/nucleon reaction and 154.0° for the 16 MeV/nucleon reaction, respectively [denoted by the arrows in Figs. 6(a) and 6(b)]. Each distribution also shows the presence of a shoulder at large angles. Given the association between linear momentum transfer and the folding angle described above, we can associate the main bump with fission following central collisions and the shoulder with fission following peripheral collisions [25]. The relative strength of the latter increases strongly with increasing fissility of the target nucleus. For the binary fission data the following observation can be made: The most probable folding angle is higher for the 22 MeV/nucleon data than for the 16 MeV/nucleon data, indicating a decreased probability for complete fusion at the higher incident energy. As the incident energy increases, the likelihood of incomplete fusion, either through projectile breakup or the onset of preequilibrium emission, increases. This trend is also consistent with the results for binary fission [25]. For the reaction at 22 MeV/nucleon, binary fission following complete fusion would correspond to an average folding angle of 152°. The most probable experimental folding angle for events associated with binary fission in nonperipheral collisions is 156.9°. This folding angle is consistent with the incomplete fusion of projectile and target nuclei followed by fission of the composite system.

Shown in Figs. 6(c) and 6(d) are the folding angle distributions associated with ternary events in which the ternary fragment has $Z \geqslant 3$ at 22 and 16 MeV, respectively. The most probable measured folding angle for ternary fission events (closed symbols) is smaller than for binary fission events [Figs. 6(a) and 6(b)]. At least in part, this decrease can be qualitatively understood as the recoil imparted to the fissioning nucleus by the backward emitted ternary particle, which boosts the fissioning nucleus in the forward direction. Open symbols indicate the distributions corrected for this trivial recoil effect. The most probable value of each distribution is indicated by the numerical values adjacent to the arrow. At 16 MeV [Figs. 6(b) and 6(d)], the average folding angle after recoil correction is essentially the same for ternary as for nonperipheral binary events. At 22 MeV [Figs. 6(a) and 6(c)], even after recoil correction, the most probable folding angle associated with ternary fission is significantly smaller than the most probable folding angle associated with binary fission.

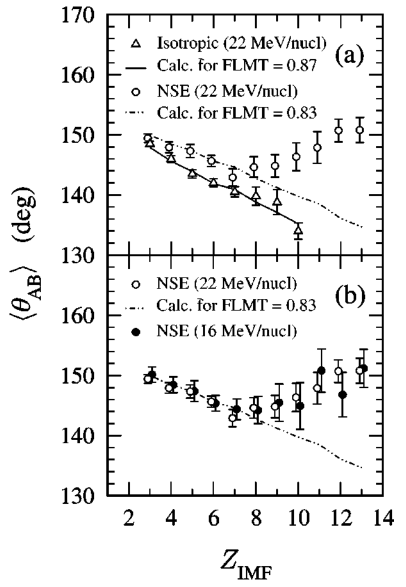

FIG. 7. Dependence of the average fission folding angle distribution on Z of the ternary particle.

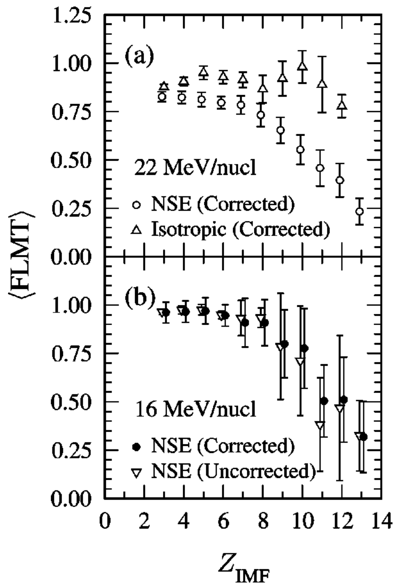

FIG. 8. Relation between the average fractional linear momentum transfer and $Z_{\rm IMF}$.

To better understand the conditions under which ternary fragments are emitted, we have examined the correlation between the average fission-fragment folding angle and the atomic number of the ternary fragment. In Fig. 7 the dependence of the average folding angle on $Z_{\rm IMF}$ of the ternary particle is presented. For isotropically emitted fragments [Fig. 7(a)], the average folding angle decreases monotonically with increasing $Z_{\rm IMF}$. As mentioned previously in connection with the bottom panels of Fig. 6, this trend is quantitatively consistent with momentum being imparted to the fissioning system by the backward emitted IMF. To examine this qualitatively, we have performed a simple calculation in which we assume the projectile transfers a given fraction of its momentum to the composite system, which then receives an additional recoil velocity consistent with the average direction and average kinetic energy of the measured ternary fragments at backward angles. The composite system then fissions with kinetic energies consistent with the systematics of total kinetic energy release in fission [5,6]. By fixing the laboratory angle of one of the fission fragments, the laboratory angle of the second fragment is calculated using the procedure described in Appendix A. The solid line in Fig. 7 corresponds to a calculation that assumes 87% linear momentum transfer from projectile to composite system followed by IMF emission and subsequent fission. The fairly good agreement between the experimental data and this simple calculation indicates that the folding angle associated with isotropically emitted fragments can be understood reasonably well within such a scenario. In contrast, IMFs emitted near scission exhibit a more complex behavior. While the folding angle for IMFs with $Z_{\rm IMF}\leqslant 7$ also decreases monotonically, as for the isotropic case, the folding angle for $Z_{\rm IMF}\geqslant 8$ increases with increasing $Z_{\rm IMF}$, suggesting that these near-scission fragments are formed in events in which less linear momentum was initially transferred to the composite system. In the lower panel of Fig. 7 the dependence of $\langle\theta_{\rm AB}\rangle$ on $Z_{\rm IMF}$ at 22 MeV is compared with 16 MeV for near-scission IMFs. The interesting behavior noted in Fig. 7(a) for near-scission emission at 22 MeV is also observed at 16 MeV. The similarity of the results for the two data sets indicates that the interesting behavior observed at $E/A=22$ MeV is not confined to a single incident energy, and that the average folding angle associated with near-scission emission is at least somewhat independent of the incident energy. We have also considered the impact of the finite (though low) detection thresholds for heavy ($Z\geqslant 8$) near-scission fragments. Low-energy fragments are necessarily associated with a small recoil to the fissioning system and hence a larger observed $\theta_{\rm AB}$. The observed increase in $\langle\theta_{\rm AB}\rangle$ for $Z_{IMF}\geqslant 8$ can thus *not* be attributed to the influence of finite detection thresholds which act to reduce the observed $\langle\theta_{\rm AB}\rangle$.

We have related the measured folding angle, $\theta_{\rm AB}$, to the fractional linear momentum transfer (FLMT) transferred by the projectile to the composite system by iteratively correcting on an event-by-event basis the recoil of the backward emitted IMFs (see Appendix A). The dependence of the average FLMT on the Z of the ternary particle is shown in Fig. 8. At 22 MeV, as displayed in Fig. 8(a), high-energy, isotropically emitted fragments are associated with a nearly constant average FLMT of ~90% within the measurement uncertainties. In contrast, the average FLMT associated with near-scission IMFs decreases monotonically from ~83% to ~25% with increasing Z. Decreasing linear momentum transfer is presumably associated with decreasing energy deposition in the composite system. Hence, the observed decrease in average FLMT with the Z of the IMFs qualitatively suggests that near-scission emission of heavy fragments is *not* driven solely by excitation energy considerations. The behavior of near-scission emission manifested in Fig. 8(a) for the 22 MeV data is also exhibited at $E/A=16$ MeV as depicted in Fig. 8(b). While the same general trend of decreasing FLMT with increasing $Z_{\rm IMF}$ is observed, at 16 MeV,

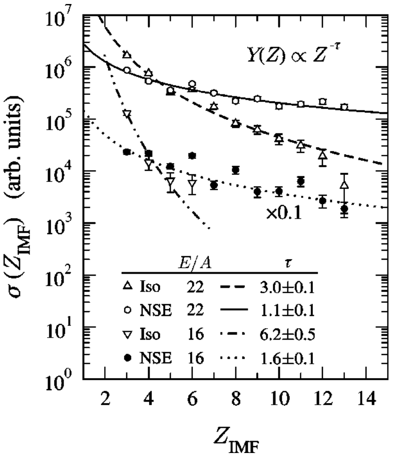

FIG. 9. Elemental yield distribution for the isotropic and near-scission emission in ternary fission events at $E/A = 16$ and 22 MeV.

for small-neck fragments, $Z_{IMF} \leqslant 6$, the FLMT is essentially 100%, in agreement with systematics. To emphasize that this trend does *not* arise as a consequence of the efficiency corrections for the finite experimental acceptance, we also present in Fig. 8(b) the ⟨FLMT⟩ uncorrected by the experimental efficiency. Data both uncorrected and corrected for the finite experimental acceptance exhibit effectively the same behavior of ⟨FLMT⟩ on Z_{IMF} indicating that the efficiency corrections play a minor role in the observed trend.

The remarkable behavior of near-scission heavy fragment emission can be further studied by observing the ternary particle yield distributions. In Fig. 9 the yield distributions of the isotropic and the near-scission components at both incident energies are shown. As evident in this figure, low-energy, near-scission emission has a relatively flat Z distribution, consistent with previous measurements [19,20]. Moreover, for heavy IMFs $(Z \geqslant 8)$ the yield distribution is essentially constant. It is instructive to compare the isotropic emission with the near-scission emission at a fixed incident energy. The near-scission Z distribution is much flatter than the corresponding distribution for isotropic emission. In the low to moderate excitation energy range examined in this work, a flatter yield distribution in a statistical emission framework is associated with higher excitation or a slower evolution of emission barriers with Z_{IMF}. Due to prior neutron emission and deformation, however, near-scission emission should be associated with lower excitation energy than the isotropic component. Consequently, the flatter yield distribution for near-scission emission again suggests a decay mode either *not* solely dependent on excitation energy or with nonstandard emission barriers. Angular momentum effects may also play a role in enhancing the probability for the emission of heavier-neck fragments consistent with the observation of a flat Z distribution. The different impact of excitation energy on isotropic emission and near-scission emission is evident in the yield distributions shown in Fig. 9. In order to compare the Z distributions presented in this figure we have fit the distributions with the form $\sigma(Z) \propto Z^{-\tau}$. On the basis of their τ value, the shape of the Z distributions for near-scission emission at 16 MeV (closed circles) and 22 MeV (open circles) are roughly comparable (1.1 and 1.6 at 22 MeV and 16 MeV, respectively). In contrast, the τ values for isotropic emission at the two incident energies is markedly different (3.0 at 22 MeV as compared to 6.2 at 16 MeV). This latter increase in τ with decreasing incident energy is consistent with a lower initial excitation energy at 16 MeV. The smaller change in τ for near-scission emission also suggests that this process is either insensitive or weakly sensitive to the excitation of the system. The influence of angular momentum on neck fragment emission may also contribute to the weak dependence of τ for the neck component at both incident energies.

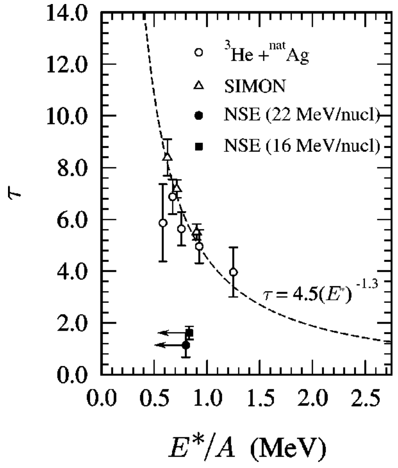

FIG. 10. Relation between the τ parameter and E^* based upon fusion-evaporation data and statistical model calculations. Solid symbols indicate the values of τ for near-scission emission.

To provide a reference frame within which to understand these extracted τ parameters, we display in Fig. 10 the parameter τ as a function of excitation energy for fusion evaporation in the reaction $^{3}\mathrm{He} + {}^{nat}\mathrm{Ag}$ at incident energies of 45–130 MeV [26]. To facilitate our comparison of this data to the NSE τ parameters extracted, we have also performed statistical model calculations with the computer code SIMON [27] and fit the predicted elemental distributions. In the simulations, the emission of light particles and clusters with $Z \leqslant 6$ were allowed to compete with fission decay of excited nuclei produced in the incomplete fusion of $^{12}\mathrm{C} + {}^{232}\mathrm{Th}$ at 22 MeV/nucleon. The open triangles in Fig. 10 display the results of the statistical model simulations. It is not surprising that a statistical model like SIMON is able to reproduce the evaporation data fairly well as the model has built in the salient features of statistical emission. The overall dependence of τ on excitation energy was determined by fitting both the experimental evaporation data and the SIMON calculations with an empirical form $\tau = a(E^*)^{-b}$ where a and b are constants. The best fit using this form is displayed as the dashed line in Fig. 10. The closed symbols in Fig. 10 which indicate the τ parameters extracted for near-scission emission in the two $^{12}\mathrm{C} + {}^{232}\mathrm{Th}$ reactions should be compared to this standard statistical evaporation reference frame. It should be noted that the deduced excitation energy for the near-scission emission case corresponds to an upper limit based on the extracted FLMT. At scission, one expects that a

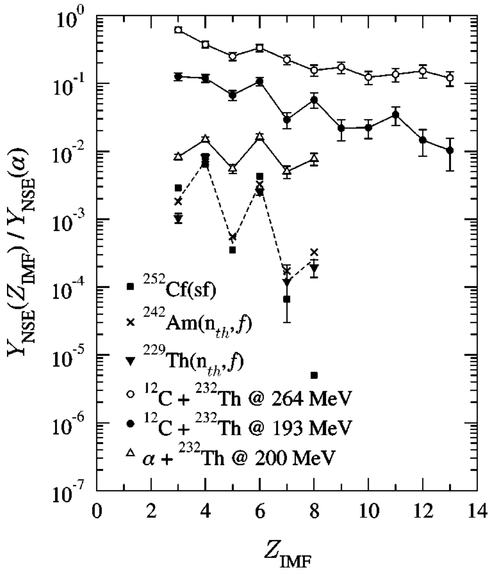

FIG. 11. Comparison of the elemental NSE yields for several different reactions. Lines serve to guide the eye.

significant fraction of the initial excitation has been converted into deformation energy or lost to prescission neutron emission. This fact is indicated in the figure by the arrows on the two near-scission emission points. However, even if we consider the initial excitation energy as the excitation energy at scission we see a marked difference for near-scission emission when compared to the points for statistical evaporation. At the same initial excitation, the value of the τ parameter for both the 22 MeV and 16 MeV data is significantly lower, by a factor of 3 or more, for the case of near-scission emission as compared to fusion evaporation. This difference suggests that the near-scission emission process cannot be described by a statistical model with emission barriers, B_{IMF}, which evolve with Z as expected for standard mononuclear emission.

Figure 11 depicts a comparison of near-scission yields for heavy-ion induced ternary fission with those reported for spontaneous and thermal neutron induced ternary fission [20,28–30]. The spontaneous and thermal neutron induced data manifest a strong odd-even effect perhaps indicating that the near-scission IMFs are being emitted when the system is at a low temperature. As the maximum available excitation energy increases (α and ^{12}C induced reactions), the magnitude of the odd-even effects which presumably arise from ground-state Q values begins to diminish. Such behavior may indicate emission from a hotter source, i.e., a higher excitation energy at scission which decreases the importance of ground-state Q-value effects. Another notable feature of the heavy-ion data is the significant yield for $Z_{\mathrm{IMF}}\geqslant 8$. This feature could result from states of higher angular momentum of the fissioning system populated by the heavy-ion reaction and may indicate the sensitivity of the near-scission emission process to angular momentum.

To explore how heavy ($Z_{\mathrm{IMF}}\geqslant 8$) fragments emitted near scission differ from those emitted isotropically, we have examined the relative yield for isotropic and near-scission fragments as a function of the excitation energy in both reactions. The average initial excitation of the composite system, prior to the emission of the ternary particle and fission, is deduced within an incomplete fusion model as explained in Appendix A. For normal statistical emission, one expects that these ratios should manifest sensitivity to the Z-dependent emission barriers. In order to explore this relationship, we have examined the yield for isotropic emission of fragments with $Z_{\mathrm{IMF}}\geqslant 4$ relative to the yield for isotropically emitted lithium as a function of the deduced excitation energy of the composite system. The results of this comparison are shown in Fig. 12(a). The experimental data exhibit an exponential increase with increasing excitation energy. This behavior can be qualitatively understood in terms of the Z dependence of the IMF emission barriers. Since the emission barrier increases with increasing Z, for a given excitation energy one observes a reduced emission probability for IMFs with larger Z. With increasing excitation energy this suppression in emission probability decreases.

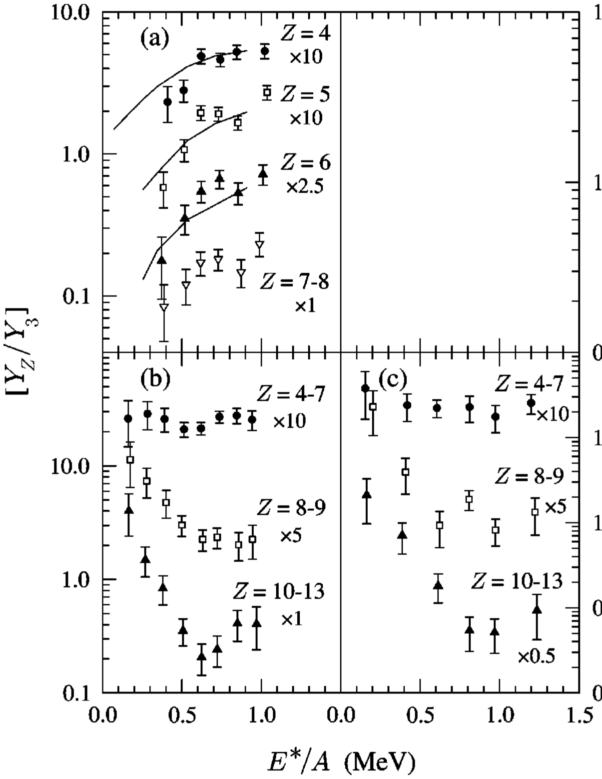

FIG. 12. Relative yield $Y(Z)/Y(3)$ as a function of E^* for the isotropic (a) and the near-scission (b) components at $E/A=22$ MeV and the NSE component at $E/A=16$ MeV (c).

We have also compared the experimental data and our simple expectations of standard statistical emission with the predictions of the statistical model SIMON. In these simulations, several cases of FLMT were selected and the initial excitation energy of the starting nucleus was estimated in the manner explained in Appendix A. In all cases, the angular momentum of the starting nucleus was assumed to be $1\hbar$. The emission of light particles and clusters with $Z\leqslant 6$ were allowed to compete with fission decay and a detection filter was developed to simulate the experimental conditions, including the energy thresholds, direction, and solid angles of all detectors. The solid lines in Fig. 12(a) depict the predicted yields of Be, B, and C relative to Li fragments as a function of excitation energy. These relative yields have been renormalized for comparison with the data. The model semiquantitatively reproduces the main trend observed in the experimental isotropic data, showing a three- to fourfold increase in the relative yield over the measured range in excitation energy. Thus, we conclude that the behavior of isotropically emitted IMFs is consistent with standard statistical emission from a compact source.

The dependence of the relative yields of near-scission emission on the initial excitation of the system at $E/A = 22$ MeV is shown in Fig. 12(b). The yields of near-scission fragments with $Z=4-7$, $Z=8-9$, and $Z=10-13$ have been normalized by the yield of $Z=3$ near-scission fragments. In marked contrast to the trends observed in panel Fig. 12(a), the relative yields in Fig. 12(b) do not show an exponentially increasing behavior with increasing excitation energy. For near-scission fragments with $Z=4-7$ the relative yield is approximately constant with increasing excitation energy. Such behavior could be understood if the emission barriers were the same or if no emission barriers existed, and would be consistent with emission of near-scission fragments from distended configurations. For $Z=8-9$ the relative yield *decreases* with increasing excitation energy. A factor of 5 decrease is observed between the cases involving the lowest excitation (peripheral collisions) and cases involving the highest excitation (more central collisions). In the case of $Z=10-13$, a suppression by a factor of approximately 20 is observed between $E^*/A=0.2$ and $E^*/A=0.6$. This trend would suggest that the emission barriers decrease as the Z of the ternary particle increases. Thus, the excitation energy dependencies of isotropic emission and near-scission emission are inherently different and may reflect the influence of angular momentum.

In understanding the association of significant near-scission heavy fragment yield with low linear momentum transfer, or equivalently low excitation energy, two points are noteworthy. First, for heavy fragments $(Z \geqslant 8)$ the mass of the fragment approaches the mass of the neck. Thus, statistical emission from the neck would require evaporation of almost the entire ‘‘source’’ and is suppressed on the basis of source size effects. Suppression of statistical emission is important if one is to clearly isolate a coexisting/competing decay mechanism. Second, for collisions involving modest linear momentum transfer ($\sim 25\%$), any deformation (stretching) introduced into the target nucleus by collision with the projectile may be significant. In contrast, central collisions should yield less deformation and greater heating of the system. Qualitative expectations dictate that survival of any initial stretching of the excited composite system into the fission channel result in a more elongated scission configuration and consequently a larger middle fragment. The survival of such an initial stretching should depend sensitively on the nature of nuclear dissipation. On this basis, one expects larger middle fragments to be associated with more stretched scission configurations, while smaller middle fragments are associated with more compact scission configurations.

TABLE IV. Experimental cross sections for near-scission emission as a function of Z_{IMF} of the ternary particle for the reaction $^{12}\mathrm{C}+^{232}\mathrm{Th}$ at 16 MeV/nucleon.

Z_{IMF}	N	N'	σ_{NSE} (mb)
3	141	232462±19577	0.118±0.023
4	138	218979±18641	0.111±0.022
5	78	123544±13989	0.063±0.013
6	116	196640±18258	0.100±0.020
7	32	53693±9492	0.027±0.007
8	36	105304±17551	0.054±0.013
9	19	40085±9196	0.021±0.006
10	23	40958±8540	0.020±0.006
11	24	63259±12913	0.032±0.009
12	13	26775±7426	0.014±0.004
13	9	17776±6295	0.010±0.004

While the approach we have used in relating the measured fission-fragment folding angle to FLMT and excitation energy is on *average* correct, for an individual event postscission emission can introduce large fluctuations in the deduced quantities. In order to assess the magnitude of these fluctuations we have utilized the Monte Carlo simulation described in Appendix B. The influence of postscission emission was emulated by smearing the fission-fragment folding angle by a Gaussian with a standard deviation of 2.8° consistent with the width of the experimentally observed ϕ_{AB} distribution. By this approach we deduce the uncertainty associated with the reconstructed excitation energy to be $\sim 20\%-25\%$. All conclusions which involve the deduced excitation energy are not affected by this level of uncertainty.

One of the important questions in studying ternary (NSE) fission is the absolute cross section of the decay channel. At $E/A=16$ MeV, the binary fission cross section was calculated by correcting the measured binary fission rate for the geometric efficiency of the setup, the dead time of the data acquisition, and the downscale factor for recording binary events. The binary fission cross section was then calculated from the corrected binary fission rate by utilizing the known intensity of the beam (integrated over several runs) and the known target thickness. By this means, the binary fission cross section in this reaction was determined to be

$$\sigma_f = 2.45 \pm 0.11 \text{ b.}$$

The cross section for IMF emission was then deduced from the efficiency corrected IMF yields and the binary fission cross section. These cross sections together with their uncertainties are listed in Table IV. For the low yields measured in this work, we estimate that the statistical uncertainties dominate the uncertainties in the calculation of the total cross section.

In the case of spontaneous or low-energy induced fission one typically expresses the relative yield for ternary fragmentation in terms of the ternary to binary ratio, $Y_{\mathrm{ternary}}/Y_{\mathrm{binary}}$. The ternary yield is dominated by the yield of light charged particles $(Z \leqslant 2)$, particularly α particles. As it has been suggested that these light particles might arise from a different production mechanism than heavier fragments [31], we choose to compare only near-scission fragments with $Z \geqslant 3$. At 16 MeV, $\sigma_{\mathrm{IMF}} = \Sigma_Z \sigma(Z) \sim 0.5$ mb, i.e., $\sigma_{\mathrm{IMF}}/\sigma_f \sim 2.3 \times 10^{-4}$. However, as the binary and ternary fission excitation functions may be different, it is perhaps more useful to compare the yield for fragments emitted near scission with $4 \leqslant Z \leqslant 8$ to the yield of near-scission lithium fragments. In the case of the ^{12}C induced reaction at 16 MeV, $Y_{\mathrm{ternary}}(4 \leqslant Z \leqslant 8)/Y_{\mathrm{ternary}}(Z=3) \sim 3.0$ while in the case of spontaneous fission of ^{252}Cf, and nth induced fission of ^{233}U, ^{235}U, and ^{242}Am, it is in the range $\sim 4-8.5$ [28–30,32]. From this comparison one can conclude that the relative yield for neck fragments with $4 \leqslant Z \leqslant 8$ is *not* significantly affected by an increase of the initial excitation energy.

IV. DYNAMICAL MODEL SIMULATIONS

In order to investigate the influence of angular momentum, isospin (N/Z), and kinetic deformation (stretching) on the ternary fission probability we utilized the Los Alamos dynamical model of fission [4]. This model was used to simulate the dynamical evolution of the system in the multidimensional deformation space as the fissioning system proceeded from saddle to scission. As this model only describes the average behavior of the system, the results are only directly comparable with data that represent the most probable decay channel, which is *not* our case. Nevertheless, these calculations are useful for qualitatively illustrating dependencies on angular momentum, N/Z, kinetic stretching, and dissipation mechanisms for ternary events even if they only involve the tail of the total cross section. Directed by our experimental measurement, special emphasis was placed on observing the onset of ternary fission.

Calculations were performed for two dissipation mechanisms: two-body viscosity (responsible for dissipation in ordinary fluids) and one-body surface dissipation (arising from collision of nucleons with the moving nuclear surface, and when there is a neck between the binary reaction partners also from transfer of nucleons through the neck). These two dissipation mechanisms represent not only opposite extremes of small and large magnitude, respectively, but also dissipations with very different tensorial properties. In order to estimate the impact of neutron emission prior to the system reaching the saddle, the fission of ^{216}U was calculated in addition to^{236}U.

The following three different situations were investigated:

(i) Compound nuclei at their saddle point with angular momenta from $\boldsymbol{l}=0$ to $\boldsymbol{l}=\boldsymbol{l}_{max}$ ($\boldsymbol{l}_{max}$ taken from the rotating liquid-drop limit); the value of the fission barrier vanishes at about $70\hbar$ for ^{236}U and $60\hbar$ for ^{216}U.

(ii) Nearly spherical systems with angular momenta greater than $\boldsymbol{l}_{max}$, representing fast-fission events.

(iii) Deformed, nonrotating, systems with large kinetic energies in the fission degree of freedom, imitating the incomplete transfer of orbital angular momentum into rigid rotation, the difference going into deformation of the composite system along the direction of the projectile impact.

In reality, of course, effects (ii) and (iii) above coexist. Figures 13 and 14 depict the effect of angular momentum on the time evolution of nuclear shapes from saddle to scission for ^{236}U and ^{216}U, respectively, under the condition of two-body dissipation. The numbers in the upper right corner of each panel indicate the time in units of 1×10^{-22} s. A viscosity coefficient $\mu = 0.02$ terapoise (TP) was used in these calculations. One can clearly see that in all cases a third light fragment forms between the two heavy fragments. The size (mass) of this fragment increases with angular momentum and is larger for ^{216}U than for ^{236}U reflecting an increase in fissility (0.697 vs 0.684).

One can likewise notice that the saddle-to-scission time also varies with angular momentum, attaining a maximum at $\boldsymbol{l}=\boldsymbol{l}_{max}$ and that it is slightly shorter for ^{216}U. The elongation at scission turns out to be the same for the two nuclei but the saddle-to-scission descent for ^{216}U is steeper than for ^{236}U. This difference leads to higher prescission dissipation and kinetic energy and consequently a shorter time scale.

The corresponding time evolution of nuclear shapes obtained with one-body surface dissipation is presented in Figs. 15 and 16. Although the time scale is now larger, the configurations are more compact and therefore no longer lead to ternary divisions. Based upon our calculations, with this type of dissipation, only the highly rotating ($120\hbar$), extremely neutron deficient ^{176}U would result in ternary fission as the average behavior.

Finally, the consequence of having a large amount of initial kinetic energy along the fission eigenvector was explored. Such a situation may occur when a significant fraction of the incident energy is neither immediately dissipated

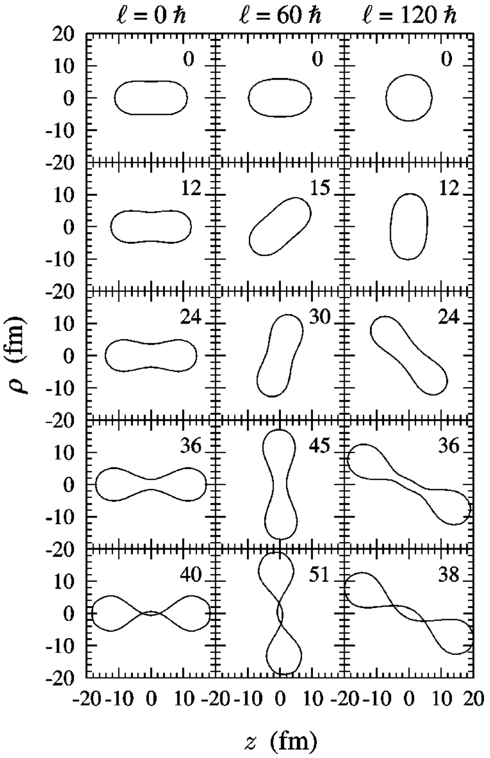

FIG. 13. Saddle-to-scission shapes calculated by a dynamical model of fission for ^{236}U at $\boldsymbol{l}=0$, 60, and 120 $\hbar$. $\mu = 0.02$ TP.

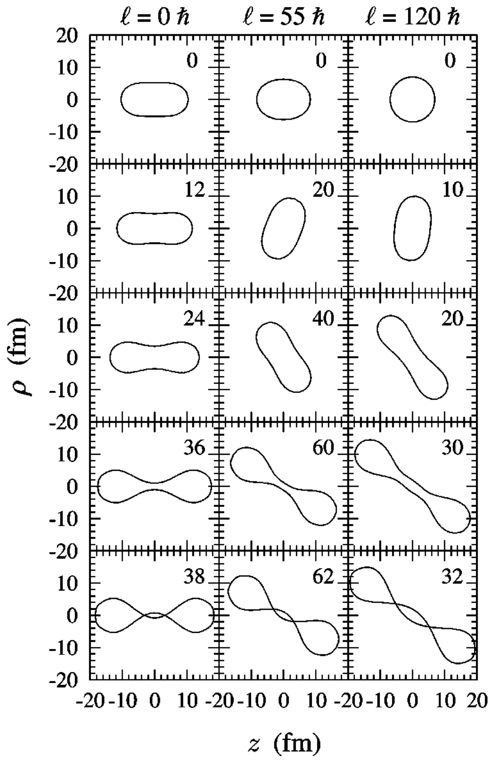

FIG. 14. Saddle-to-scission shapes calculated by a dynamical model of fission for ^{216}U at $\boldsymbol{l}=0,55$, and 120 $\hbar$. $\mu=0.02$ TP.

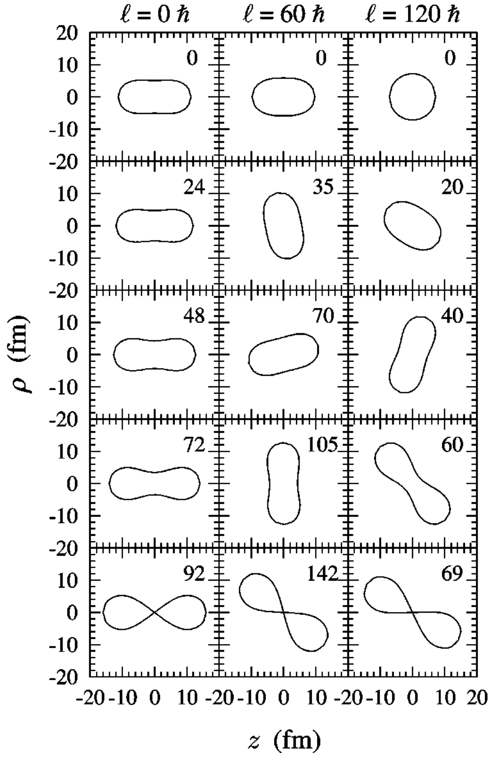

FIG. 15. Saddle-to-scission shapes calculated by a dynamical model of fission for ^{236}U at $\boldsymbol{l}=0,60$, and 120 $\hbar$ with one-body dissipation.

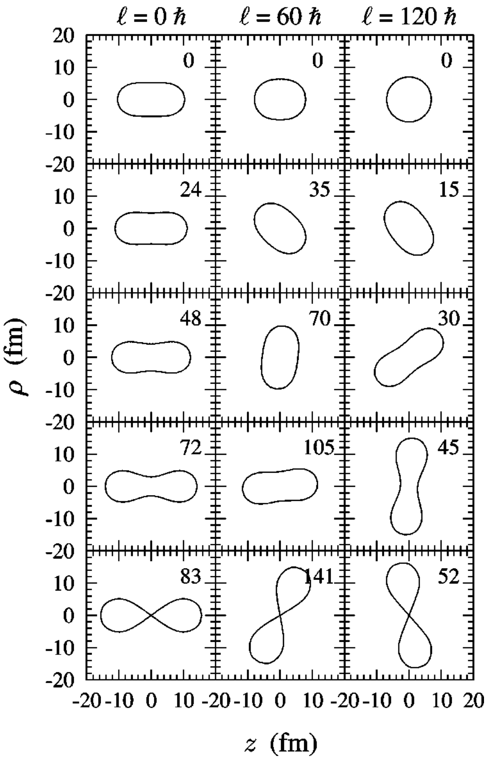

FIG. 16. Saddle-to-scission shapes calculated by a dynamical model of fission for ^{216}U at $\boldsymbol{l}=0,60$, and 120 $\hbar$ with one-body dissipation.

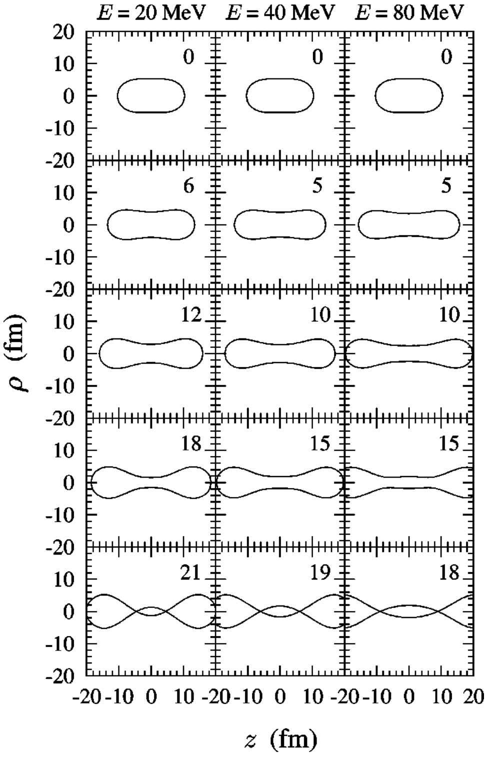

FIG. 17. Saddle-to-scission shapes calculated by a dynamical model of fission for ^{216}U at $E=20$, 40, and 80 MeV with two-body dissipation.

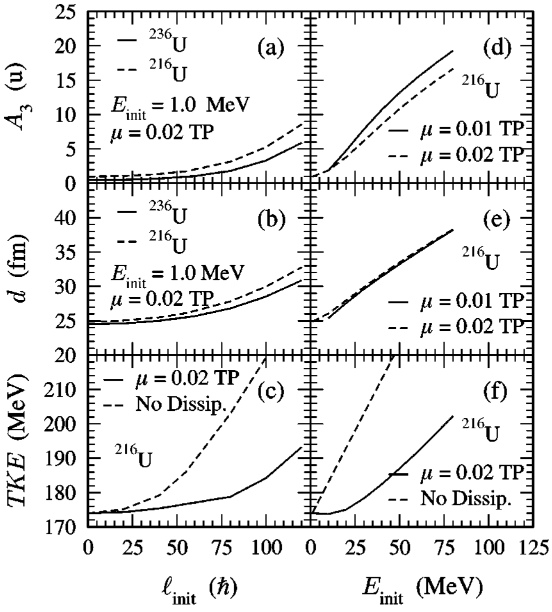

FIG. 18. Summary of the Los Alamos dynamical fission model calculations assuming two-body dissipation.

nor converted into rigid rotation but instead deforms the system along the direction of the projectile motion. This motion will be largely converted into motion along the scission axis. Shown in Fig. 17 are the results for two-body dissipation and $\boldsymbol{l}=0$. The ability of the system to attain even larger middle fragments than previously calculated is remarkable. For the case of two-body dissipation, a large kinetic energy along the fission direction is indeed an efficient means to produce ternary fragmentations. In contrast, for the case of one-body dissipation the initial kinetic energy is quickly damped into intrinsic excitation. For this case, therefore, initial stretching does not result in an increased ternary probability.

A summary of our calculations is provided in Fig. 18. In this figure, the influence of angular momentum or initial kinetic energy on the size of the middle fragment, the distance between the two-fission fragments, and the total kinetic energy is depicted for the case of two-body dissipation. As the angular momentum increases [Figs. 18(a)–18(c)], all three quantities increase. For $\boldsymbol{l} \leqslant \boldsymbol{l}_{max}$, the increase is moderate, however, in contrast to the increase for angular momenta above the rotating liquid-drop limit. For a fixed value of the angular momentum, the neutron deficient nucleus ^{216}U exhibits a slight increase in the mass of the middle fragment, accompanied by slightly larger fission-fragment separation, as compared to ^{236}U. The behavior of the size of the middle fragment, the fission-fragment separation, and the total kinetic energy on the initial kinetic energy is relatively linear as a function of the initial stretching energy E_{init} [Figs. 18(d)–18(f)]. The magnitude of the two-body coefficient has a modest effect on the size of the middle fragment [Fig. 18(d)] while providing little change in the fission-fragment separation distance [Fig. 18(e)]. Shown explicitly in Fig. 18(f) is the effect of dissipation on the total kinetic energy of the fragments. Under the assumption of two-body dissipation with $\mu=0.02$ TP, the initial kinetic energy in the fission direction results in a measurable increase in the total kinetic energy of the fission fragments. Measurement of the kinetic energies of the fission fragments in future experiments should thus allow one to determine if ternary fragmentations are associated with a different amount of dissipation as compared to binary fission or whether they follow Viola fission systematics.

As far as the comparison of these dynamical calculations with the present measurements is concerned, we have noticed that while the two-body dissipation predicts too much ternary fission, the one-body dissipation does not predict enough. From these results we may conclude that the actual mechanism is an intermediate one that includes not only one-body collisions but to a lesser extent also two-body collisions. In such a scenario, ternary fission will not appear as the main channel but in the tail of the total cross section with characteristics similar to those calculated above.

V. STATISTICAL INTERPRETATION OF EXPERIMENTAL RESULTS

It has recently been suggested that the results obtained in this work can be understood within a statistical emission framework [33]. If, based on a statistical description one writes the probability of emitting a fragment with atomic number Z as

$$P_Z \propto A_Z e^{-B_Z/T},$$

where B_Z represents the barrier for emission of the particle and T is the temperature of the system, then one can express the relative probability

$$P_Z/P_3 = K_Z e^{-(B_Z-B_3)/T} = K_Z e^{-\Delta B/T},$$

$$\ln(P_Z/P_3) = \ln(K_Z) - \Delta B/T = \ln(K_Z) - \sqrt{a/E^*}\,\Delta B, \quad (2)$$

where $\Delta B = B_Z - B_3$, E^* is the excitation energy of the system, a is its level density parameter, and $K_Z = A_Z/A_3$. We have assumed for this heuristic calculation that the change in a is only marginally affected by mass loss.

For a statistical process for which a is constant we expect an exponential dependence on $1/E^*$. Isotropically emitted fragments in the 22 MeV/nucleon data have been shown to follow such a dependence. In such an analysis, the quantity ΔB associated with isotropically emitted fragments is a positive number indicating that $B_Z > B_3$ as expected. In contrast, for near-scission emission, $\Delta B < 0$. This result implies that $B_Z < B_3$, in effect that the emission barriers decrease with increasing Z [33]. One can speculate that such a dependence implies that larger middle fragments arise from more stretched, thin-necked configurations while smaller middle fragments originate from shorter thick-necked configurations. As thin necks presumably require less energy to rupture, the larger middle fragments are associated with lower emission barriers.

Whether such a statistical approach is justified, however, is questionable [34]. For near-scission emission to be viewed as a "normal" statistical process albeit one with nonstandard emission barriers, it is important that one ascertain whether the modes leading to neck rupture are populated with the appropriate statistical weight. As such an analysis is lacking it is premature to label the near-scission process statistical. Moreover, in relating the excitation energy to a statistical temperature it is important to recall that the excitation energy deduced from the measured linear momentum transfer is at best the *initial* excitation of the system. For the isotropically emitted fragments, which are emitted early prior to deformation or prescission emission, this initial excitation energy should correspond closely to the excitation at the time of emission. The excitation functions observed in Fig. 12 indicate that this expectation is valid.

On the other hand, when fragments are emitted later, near scission, the initial excitation is more weakly related to the emission probability. It is important to realize that the measured fractional linear momentum transfer, from which the excitation was deduced, is also related to the impact parameter, b, or the angular momentum, $\boldsymbol{l}$, of the collision. Smaller linear momentum transfers (smaller deduced initial excitation) are associated with more peripheral collisions, and larger linear momentum transfers (larger deduced initial excitation) are associated with more central collisions. As indicated by our calculations with the Los Alamos dynamical model, angular momentum and kinetic stretching can influence ternary fission. These calculations suggest that the scission configuration may be sensitively related to the incoming angular momentum wave. Whether different scission configurations can be described by the same level density parameter as assumed in this statistical treatment is questionable.

VI. SUMMARY AND CONCLUSIONS

We have examined the characteristics of IMFs emitted on a time scale prior to and commensurate with fission following incomplete fusion reactions. IMFs emitted early, prior to substantial deformation, exhibit an isotropic emission pattern and have relatively high kinetic energies. We also observe low-energy IMFs, focused approximately orthogonal to the scission axis—two signatures of near-scission emission. We have studied and compared the characteristics of these two types of emission in order to determine if they exhibit substantive differences. For near-scission emission we find that $\langle E_{\mathrm{c.m.}} \rangle$ as a function of Z_{IMF} is essentially the same for both incident energies studied as well as nth induced ternary fission. This observation suggests that either $\langle E_{\mathrm{c.m.}} \rangle$ is insensitive to the excitation of the system or the excitation at the time of scission is comparable. A striking feature readily discernible is the difference in the Z distributions for the two types of emission. Near-scission emission is associated with a much flatter Z distribution than isotropic emission, inconsistent with excitation driven emission with standard emission barriers. While the Z distributions for isotropic emission at $E/A = 16$ and 22 MeV are significantly different ($\tau = 3.0$ and 6.2), we find rather similar Z distributions for near-scission emission at both energies ($\tau = 1.1$ and 1.6). Comparison with a standard statistical model and fusion-evaporation data indicates that either emission barriers are significantly different for near-scission emission or the Z distribution for this process is largely determined by dynamics rather than statistical decay. A remarkable aspect of the ^{12}C induced reactions is the yield for heavy ternary fragments ($Z_{\mathrm{IMF}} > 8$) in near-scission emission compared to spontaneous and low-energy ternary fission. We have also examined the correlations between IMF emission and the folding angle of the two fission fragments. From the measured folding angle, we deduced the fractional linear momentum transfer and the excitation energy of the fissioning system. By examining the relative probabilities of IMF emission as a function of excitation energy, we deduced that the near-scission component and the isotropic component behave inherently differently. In the case of isotropic emission the relative yields for different Z fragments can be understood in terms of emission barriers which increase with increasing Z. In contrast, the mechanism of near-scission emission must be one for which the barriers are intimately related to the trajectories which undoubtedly are determined to a large extent by the incoming partial wave. While it is undoubtedly true that such trajectory-dependent barriers, along with the thermalized energy, determine the absolute yield of the neck IMFs it is not at all clear to what extent the size of the near-scission fragment is determined by the incoming partial wave. On the theoretical side, we have explored the dependence of the ternary fission on N/Z, angular momentum, and kinetic deformation, with the Los Alamos model. Depending on the dissipation, large angular momenta or initial kinetic stretching can have a significant impact on the size of the ternary fragment. As the Los Alamos model only treats the most probable behavior while experimentally ternary fission remains a rare process, a theoretical treatment which includes shape fluctuations is required in order to make a more direct and meaningful comparison.

APPENDIX A: KINEMATIC RECONSTRUCTION

An iterative, self-consistent method was developed for the kinematic reconstruction of binary and ternary fission events. The fission-fragment folding angle technique [35] was used for both event types to deduce the velocity of the putative composite nucleus v_{CN}, from which several quantities of interest, including the fractional linear momentum transfer (FLMT) from the projectile to the resulting composite system and its initial excitation energy, were deduced within the framework of an incomplete fusion model. In ternary fission events the kinematic reconstruction has to account for the recoil given to the residual composite system after emission of a third lighter particle, which in this context is called the fissioning nucleus to make a clear distinction between the system prior to the emission, the composite nucleus. Since isotropic and near-scission emission occur either prior to or concurrent with fission, they can be treated simultaneously with no distinction. Figure 19 shows the velocity vector diagram for binary fission and fission accompanied by a third particle. The velocity of the composite nucleus, prior to the emission and fission, is assumed to be along the beam line. Primed quantities are evaluated in the rest frame of the fissioning nucleus. For binary fission, the following equations can be derived using trivial trigonometric identities,

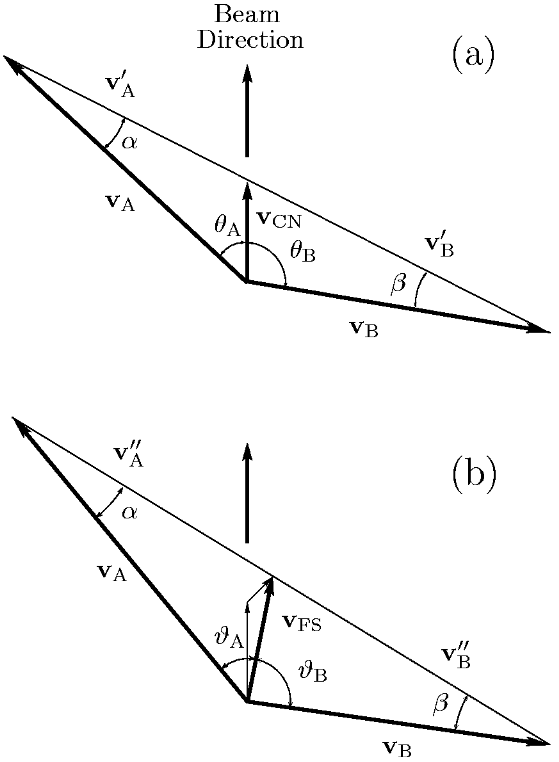

FIG. 19. Velocity vector diagram explaining the kinematic reconstruction for binary (a) and ternary (b) fission.

$$(v'_B)^2 = v_{CN}^2 + v_B^2 - 2 v_{CN} v_B \cos\theta_B, \tag{A1}$$

$$v_B = (v'_A + v'_B)\frac{\sin\alpha}{\sin\theta_{AB}} = v_{CN}\left(1 + \frac{v'_B}{v'_A}\right)\frac{\sin\theta_A}{\sin\theta_{AB}} = v_{CN}\kappa\xi, \tag{A2}$$

where

$$\xi = \frac{\sin\theta_A}{\sin\theta_{AB}}, \tag{A3}$$

$$\kappa = 1 + \frac{v'_B}{v'_A} = 1 + \frac{v_A \sin\theta_A}{v_B \sin\theta_B}, \tag{A4}$$

and θ_{AB} is the folding angle. Hence, Eq. (A1) can be put into a second order equation in ξ,

$$\xi^2 - \frac{2\cos\theta_B}{\kappa}\xi + \frac{1}{\kappa^2}\left[1 - \left(\frac{v'_B}{v_{CN}}\right)^2\right] = 0, \tag{A5}$$

which has the solution

$$\xi = \frac{1}{\kappa}\left(\cos\theta_B \pm \sqrt{\cos^2\theta_B - \left[1 - \left(\frac{v'_B}{v_{CN}}\right)^2\right]}\right). \tag{A6}$$

Furthermore, from Eq. (A3) it is easy to derive the following relation:

$$\tan\theta_A = \frac{\xi\sin\theta_B}{1 - \xi\cos\theta_B}. \tag{A7}$$

Equation (A7) is an expression for the angle of one fragment in terms of quantities related to the other fragment. Known quantities are v_A, v_B, θ_A, and θ_B, while v'_B and v_{CN} are unknown. However, v'_B can be evaluated using the systematics of total kinetic energy (TKE) release in fission [5,6],

$$\mathrm{TKE} = 0.755\frac{Z_A Z_B}{A_A^{1/3} + A_B^{1/3}} + 7.3\ \mathrm{MeV}. \tag{A8}$$

The mass and charge of the fission fragments are unknown. However, momentum conservation in the fission process requires that $v'_B/v'_A = m_A/m_B$. Hence, the fission-fragment mass ratio can be estimated using Eq. (A4). Equations (A6) and (A7) are applicable to ternary fission events if one replaces v_{CN} with the velocity of the fissioning system v_{FS}, θ_A with ϑ_A and θ_B with ϑ_B. This case is equivalent to a simple rotation of the velocity vectors by the angle between v_{FS} and the beam line.

At the beginning of the procedure, initial values are chosen for the mass number and atomic number, A_{CN} and Z_{CN}, as well as the velocity $v_{CN} = v_0$ of the composite nucleus, consistent with the complete fusion of the projectile and target. Then the momentum components of the ternary particle in the rest frame of the composite nucleus are calculated (the laboratory momentum components are measured quantities) which, by momentum conservation, gives the recoil momentum vector given to the composite nucleus. The recoil velocity in the rest frame of the composite nucleus is then evaluated taking into account the loss of mass after the emission of the third particle, and the velocity of the fissioning nucleus v_{FS} in the laboratory system is constructed by adding vectorially the recoil velocity to v_{CN}. No such correction is made for binary fission events. Next, v'_B is calculated using Eq. (A8) with fission masses estimated using the mass ratio and the choice of mass of the fissioning system. In the case of binary fission, the total fissioning mass is A_{CN} and in the case of ternary fission $A_{FS} = A_{CN} - a$, where a is the mass number of the ternary particle, a known quantity. The fission-fragment charges are estimated assuming they have the same N/Z ratio as the fissioning system.

The folding angle is calculated with Eq. (A7) using the measured angle θ_B (or ϑ_B in case of ternary fission) and assuming θ_A (or ϑ_A) is unknown. This folding angle is compared with the experimental folding angle, having in mind that

$$\theta_A + \theta_B = \vartheta_A + \vartheta_B = \theta_{AB}. \tag{A9}$$

If the calculated θ_{AB} does not agree with the experimental value, v_{CN} is increased or decreased depending on whether the calculated θ_{AB} is larger or smaller than the experimental value, respectively, and the procedure is repeated until there is convergence.

If $\eta = v_{CN}/v_0$, where v_{CN} is the parallel-to-the-beam recoil velocity of the composite nucleus and v_0 the complete fusion velocity, then

$$\text{FLMT} = \eta \frac{1}{1+\frac{A_p}{A_t}(1-\eta)} \equiv \rho \tag{A10}$$

in an incomplete fusion model. A_p and A_t are the projectile and target mass numbers, respectively. Hence, the deduced value of $v_{\rm CN}$ obtained above can be used to calculate the FLMT. However, in the incomplete fusion model the mass and charge of the composite nucleus can be taken as $A_{\rm CN} = \rho A_p + A_t$ and $Z_{\rm CN} = \rho Z_p + Z_t$. Hence, the initial choice of $A_{\rm CN}$ and $Z_{\rm CN}$ has to be modified, and the whole procedure repeated until this second iteration reaches convergence. The procedure renders the FLMT to the primary composite system prior to the emission of the ternary particle and fission. Evaporation of light particles from the composite system prior and after emission of the ternary particle is neglected.

Within the framework of the incomplete fusion model the average excitation energy consistent with a given FLMT can be written

$$\langle E^* \rangle = E_p \rho \frac{A_t}{A_t + \rho A_p} \sqrt{1 - \left(\frac{v_p}{c}\right)^2} + \langle Q \rangle, \tag{A11}$$

where E_p is the projectile energy, v_p is the velocity of the projectile, and $\langle Q \rangle$ is the average Q value of reaction channels consistent with the given ρ. Here we take the part of the projectile that is not transfered $(1-\rho)A_p$ and consider all possible combinations of reaction channels leading to a loss of nucleons or clusters of nucleons and take the average of their Q values. Hence, we may associate a $\langle E^* \rangle$ with a FLMT. We further tested the consistency of the procedure by assuming the evaporation of neutrons removed on average 10 MeV of the primary excitation energy and reduced the mass of the fissioning nucleus as if neutron emission exhausted the excitation energy. Very little, if any, difference was observed in the deduced FLMT.

APPENDIX B: EFFICIENCY CALCULATIONS

The geometric efficiency of the experimental setup was determined by utilizing a Monte Carlo program. The main factors accounted for by this program were (i) the width of the FLMT distribution which depends on the ternary particle Z_{IMF}, (ii) the recoil effect of the ternary particle on the two fission fragments, (iii) the angular distribution of the ternary particle with respect to the scission axis, and (iv) the dispersion in angular correlations both in plane and out of plane due to postscission particle emission.

The initial step in the efficiency calculation was to sample the experimentally measured Z distribution. The mass number (A) of the ternary fragment was then estimated by relating the measured Z to A in accordance with previous measurements of ternary fission [20,21]. The energy of the ternary particle was based upon the experimentally measured kinetic energy spectra converted to the center of mass.

We assumed that all values of FLMT were equally probable. The FLMT was then related to the velocity of the composite nucleus within the context of a massive transfer model and deduced a self-consistent (Z,A) for the composite system. For the somewhat excited nuclei undergoing fission in this experiment we assumed that symmetric fission was the most probable outcome. In order to account for the full range of mass splits possible we utilized the width of the fission mass distribution deduced from the reconstructed experimental data to select the (Z,A) of the two fission fragments. The TKE for the ternary fission was assumed to follow Viola systematics and together with momentum conservation provided the center-of-mass velocities of the fission fragments. The angular distribution of the ternary IMF was assumed to be well described by the angular correlation previously measured for ternary alpha particles [36]. We further assumed axial symmetry of the ternary particle with respect to the scission axis. This assumption is reasonable for a particle emitted near the center of mass. In this case, the particle is insensitive to the angular momentum of the system and no in-plane enhancement is observed. Postscission emission of neutrons which alters the direction of the two fission fragments was simulated by smearing the direction of the fission fragments with a Gaussian. The standard deviation of this Gaussian was taken to be 2.8° consistent with the out-of-plane dispersion ($\Delta\phi$) depicted in Fig. 5. The coordinate system which describes this three-body breakup was then transformed so as to account for the isotropic decay of the fission process. Events simulated in this manner were then filtered by a software representation of the experimental setup in order to determine the geometric efficiency.

[1] U. Brosa and S. Grossmann, Z. Phys. A **310**, 177 (1983).

[2] U. Brosa and S. Grossmann, J. Phys. G **10**, 933 (1984).

[3] U. Brosa, S. Grossmann, A. Müller, and E. Becker, Nucl. Phys. **A502**, 423c (1989).

[4] N. Cârjan, A. Sierk, and J. Nix, Nucl. Phys. **A452**, 381 (1986).

[5] V. Viola, Nucl. Data Tables **A1**, 391 (1966).

[6] V.E. Viola, K. Kwiatkowski, and M. Walker, Phys. Rev. C **31**, 1550 (1985).

[7] D. Hinde *et al.*, Phys. Rev. C **45**, 1229 (1992).

[8] P. Paul and M. Thoennessen, Annu. Rev. Nucl. Sci. **44**, 65 (1994).

[9] I. Dioszegi, N.P. Shaw, I. Mazumdar, A. Hatzikoutelis, and P. Paul, Phys. Rev. C **61**, 024613 (2000).

[10] A. Rindi, V. Perez-Mendez, and R.I. Wallace, Nucl. Instrum. Methods **77**, 325 (1970).

[11] J.R. Gilland and J.G. Emming, Nucl. Instrum. Methods **104**, 241 (1972).

[12] T.A. Bredeweg, Ph.D. thesis, Indiana University, 2001.

[13] U. Lynen *et al.*, Nucl. Phys. **A409**, 385c (1983).

[14] K. Kwiatkowski *et al.*, Nucl. Instrum. Methods Phys. Res. A **299**, 166 (1990).

[15] D. Fox *et al.*, Nucl. Instrum. Methods Phys. Res. A **368**, 709 (1996).

[16] J. Ziegler, computer code TRIM91, IBM-Research, Yorktown, NY 10598, USA, 1983.

[17] J. Ziegler, J. Biersack, and U. Littmark, *The Stopping and Range of Ions in Solids* (Pergamon, New York, 1985).

[18] M.W. Sachs *et al.*, Nucl. Instrum. Methods **41**, 213 (1966).

[19] D. Fields *et al.*, Phys. Rev. Lett. **69**, 3713 (1992).

[20] S. Chen *et al.*, Phys. Rev. C **54**, 2114 (1996).

[21] M. Mutterer and J.P. Theobald, in *Nuclear Decay Modes*, edited by D. Poenaru (Institute of Physics, University of Reading, Berkshire, 1996), pp. 487–530.

[22] L.G. Moretto, K.X. Jing, L. Phair, and G.J. Wozniak, J. Phys. G **23**, 1323 (1997).

[23] R.J. Charity, Phys. Rev. C **61**, 054614 (2000).

[24] V. Viola *et al.*, Phys. Rev. C **26**, 178 (1982).

[25] V. Viola, Nucl. Phys. **A471**, 53c (1987).

[26] M. McMahan *et al.*, Phys. Rev. Lett. **54**, 1995 (1985).

[27] D. Durand, Nucl. Phys. **A541**, 266 (1992).

[28] Y. Gazit, E. Nardi, and S. Katcoff, Phys. Rev. C **1**, 2101 (1970).

[29] W. Baum, Ph.D. thesis, Technische Hochschule Darmstadt, 1992.

[30] M. Wöstheinrich *et al.*, Acta Phys. Slov. **49**, 117 (1999).

[31] N. Carjan, J. Phys. (France) **37**, 1279 (1976).

[32] A.A. Vorobiev *et al.*, Phys. Lett. **B30**, 332 (1969).

[33] L.G. Moretto, D. Breus, L. Phair, and G.J. Wozniak, Phys. Rev. Lett. **85**, 2645 (2000).

[34] R. Yanez *et al.*, Phys. Rev. Lett. **85**, 2646 (2000).

[35] T. Sikkeland, E.L. Haines, and V.E. Viola, Phys. Rev. **125**, 1350 (1962).

[36] J.P. Theobald, P. Heeg, and M. Mutterer, Nucl. Phys. **A502**, 343c (1989).